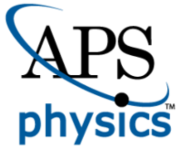

CHORUS

This is the accepted manuscript made available via CHORUS. The article has been published as:

Infrared ultrafast spectroscopy of solution-grown thin film tellurium

Vasudevan Iyer, Mauricio Segovia, Yixiu Wang, Wenzhuo Wu, Peide Ye, and Xianfan Xu

Phys. Rev. B **100**, 075436 — Published 28 August 2019

DOI: 10.1103/PhysRevB.100.075436

Infrared ultrafast spectroscopy of solution grown thin film tellurium

Vasudevan Iyer[1], Mauricio Segovia[1], Yixiu Wang[2], Wenzhuo Wu[2], Peide Ye[3], and Xianfan Xu[1]*

[1]*School of Mechanical Engineering and Birck Nanotechnology Center, Purdue University, West Lafayette, 47907, USA*

[2]*School of Industrial Engineering, Purdue University, West Lafayette, 47907, USA*

[3]*School of Electrical Engineering and Birck Nanotechnology Center, Purdue University, West Lafayette, 47907, USA*

Several materials studied intensively in their bulk forms several decades ago have re-emerged in recent years in their thin film and monolayer manifestations. Tellurium, like black phosphorus, is one such elemental two-dimensional material with promising semiconducting properties for electronic and optoelectronic applications. To study the fundamental carrier properties such as hot carrier relaxation and recombination, we performed ultrafast femtosecond pump-probe spectroscopy on thin flakes of solution grown tellurium. To access the low bandgap of tellurium, we used infrared, near band-gap and below bandgap probes to monitor the relaxation processes. Sweeping the probing wavelengths across the bandgap helps to shed light on the anisotropic band structure of the material. We find that relaxation in flakes of 60-160 nm thickness is on the order of 100s of pico-seconds. Thinner flakes (10-20 nm), on the other hand, exhibit fast relaxation times of sub 20 ps. Radiative recombination is identified as the relaxation mechanism in thick flakes whereas mid-gap trap states arising from surface defects and impurities are responsible for the fast relaxation in thin flakes. A diffusion-recombination model accounting for the surface defect and radiative recombinations explain the experimental data well.

With ever increasing demands on the performance, robustness and speed of electronic and computing devices, there is a search for novel materials to continue the Moore's law into the next decade. To this end,

Email correspondence to: xxu@ecn.purdue.edu

two-dimensional (2D) materials are being intensely studied to ascertain their utility for next generation of transistors, photodetectors, interconnects and a host of other components [1–3]. After several successful applications of graphene [4,5], its limited performance in transistors due to lack of band gap [6] lead to investigation and discovery of many other 2D materials such as transition metal dichalcogenides [7], black phosphorus [8,9], and topological insulators [10]. Even these new materials suffered from some limitations. For example, transition metal dichalcogenides exhibit low electron/hole mobilities in general [11,12] and black phosphorus is unstable in air due to oxidation [13]. The enhanced properties of topological insulator surface states could not be harnessed to their full potential due to bulk contribution [14]. Another major challenge is the fabrication of these 2D materials on a large scale, with extensive efforts being invested in techniques such as chemical vapor deposition [15], molecular beam epitaxy [16], and liquid phase exfoliation [17]. Only a few materials such as some transition metal dichalcogenides and graphene are being produced on wafer scale [18,19].

A recent 2D material, 2D tellurium, has emerged as a promising candidate for electronic and optoelectronic applications. A novel substrate free solution growth method has been developed which facilitates controllable flake thickness [20,21]. Moreover, using the Langmuir–Blodgett process and ink-jet printing, the flakes can be assembled to obtain large area samples [20]. Apart from the feasibility of scalable growth, tellurium transistors have been shown to exhibit high mobility, good on/off ratio, and large drain current [20,22–24]. Furthermore, the bandgap is thickness tunable, which could prove useful in tunable light absorption [20]. Finally, the material is air stable without the need for encapsulation [20], thus overcoming many of limitations discussed previously. A more detailed description of the properties of this material can be found in a recent review [25]. Due to the rising interest in this material, it is important to understand the fundamental electron/hole carrier dynamics which directly impacts the performance of devices. Ultrafast pump-probe spectroscopy is a useful tool to investigate hot carrier dynamics, carrier scattering and recombination in a variety of materials such as nanoparticles [26], quantum dots [27],

metals [28], and 2D materials [29,30]. There have been ultrafast studies on the coherent phonon dynamics in bulk tellurium crystals [31,32], but no studies on the near bandgap and free carrier dynamics on thin films to the best of our knowledge. Since most devices rely on near band edge phenomena, it is essential to understand the infrared transient response of the material, which can access the small bandgap of 0.35 eV [33].

The tellurium flakes were synthesized using the substrate free solution growth method [20], and the suspended flakes were scooped out from the solution onto a CaF_2 substrate with pre-deposited gold location markers (see Supplementary note 1 [34]). The flakes were identified with an optical microscope (Fig. 1a), followed by collecting a Raman spectrum (Horiba LabRAM, Fig. 1b) to determine the flake orientation [20] (see Supplementary note 2 [34] and references [35,36] therein). The red arrow in Fig. 1a is the direction perpendicular to the c-axis (or parallel to $[1\bar{2}10]$ axis) and the blue arrow is parallel to the c-axis ($[0001]$ axis). An AFM scan was done to determine the thickness. FTIR (Fourier-Transform Infrared Spectroscopy) transmission scans were also performed using an FTIR microscope (Thermo Fisher Scientific, Continuum) as shown in Fig. 1c for three flakes of thickness 14, 60 and 160 nm. The point where the slope changes in the 160 nm flake, indicated by the intersected straight line in Fig. 1c, corresponds to the bandgap of 0.35 eV. The 14 nm flake shows weak hump like features near 0.3 eV, which could be due to many body effects such as excitons. A recent study theoretically predicted exciton binding energy of up to 670 meV in monolayer suspended tellurium, and decreased strength for supported samples and thicker films [37]. Detailed thickness dependent photoluminescence excitation spectroscopy [38,39] could reveal more details and is beyond the scope of this work. Bulk flakes were predicted to have <10 meV binding energy at room temperature and hence we have neglected excitonic effects in our analysis for >20 nm flakes. More discussion on <20 nm samples will be provided later. Ultrafast pump-probe transmission spectroscopy was carried out on the flakes (see Supplementary note 3 [34] for experimental details). The change in transmission ($\Delta T/T$) at a pump-and-probe delay time of 7 ps, for a 130 nm flake, with the probe

wavelength varying across the bandgap, is shown in Fig. 1d. The pump and probe were both either polarized along the c-axis (|| c) or perpendicular to the c-axis (⊥ c). The transmission data for light polarization perpendicular to the c-axis is more indicative to the bandgap, as has been observed previously in literature for bulk crystal [33]. The photo generated carriers accumulate near the band edge, hence there is a larger change in the transmission of the probe when its wavelength is tuned close to the bandgap. The change of transmission vs. wavelength can be seen clearer by fitting a spline curve through the experimental data points by performing a numerical differentiation [40] to obtain the point of maximum, which is indicated by the black dashed line at 0.355 eV. The pump and probe were polarized perpendicular to the c-axis in the remainder of the manuscript.

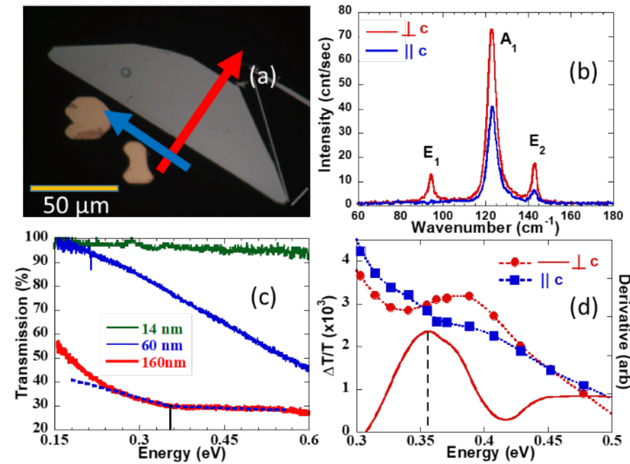

Fig. 1: Characterization of a 130 nm flake using (a) optical microscopy and (b) Raman spectroscopy to determine orientation. (c) FTIR transmission for flakes with various thicknesses. The change in the slope of the curve for the 160 nm flake corresponds to the bandgap of 0.35 eV. (d) The change in transmission at 7 ps delay for a 130 nm flake as a function of energy for pump and probe polarizations either oriented perpendicular or parallel to the c-axis, with spline fits (dotted lines) and its derivative (solid line). The band edge near 0.35 eV is clearly discernable for light polarization perpendicular to the c-axis.

The relaxation dynamics of 40 to 160 nm flakes following excitation by the 800 nm (1.55 eV) pump beam is shown in Fig. 2a for a bandedge probe wavelength of 3500 nm (0.35eV). The pump fluence is 0.02

mJ/cm^2. Results with 5800 nm (0.21 eV) probe are provided in Supplementary note 4 [34], Fig. S1. Fluence dependent dynamics for 130 nm flake are shown in Fig 2b. The recombination dynamics in tellurium has been studied previously using steady state [41] and transient photoconductivity [42], as well as transient microwave conductivity [43]. These studies did not have the time-resolution to determine the recombination time at room temperature. The reported values at low temperature (77 K) range in the 10s of ns to microsecond regime and the authors predicted room temperature recombination time to be several orders smaller than at low temperature. A recent study on recombination dynamics in powdered tellurium obtained few nanosecond lifetimes at room temperature using transient microwave conductivity with a minimum time resolution of 300 ps [44]. Our measurements are the first on thin film tellurium with sub-picosecond time resolution.

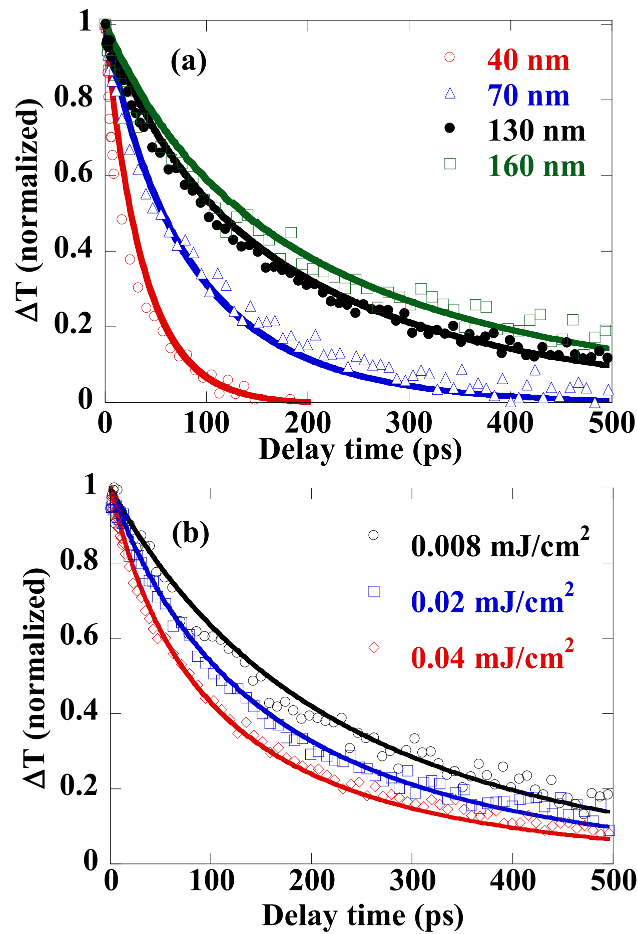

Fig. 2: (a) Relaxation dynamics in 40 to 160 nm flakes following excitation by 800 nm pump and probing with 3500 nm. The transient curves are normalized, and the point of maximum signal is set as delay time of 0 ps. The solid lines are obtained from diffusion-recombination model simulations. (b) Fluence dependent measurements on a 130 nm flake along with simulation curves.

A diffusion-recombination model (see Supplementary note 5 [34], and reference [45] therein) was used to simulate the dynamics as shown by the solid lines in Fig 2a and 2b. Several recombination mechanisms have been proposed for bulk tellurium in literature such as direct recombination [41], trap/defect states near the band edge [42], mid-gap trap states [43], and point defects and dislocations [46]. The TEM cross section of the flakes in a previous study revealed good quality of the flakes in the bulk and hence point defects and dislocations are less likely [20]. Therefore radiative or SRH (Shockley-Read-Hall, trap assisted) recombination are the more probable recombination routes, as was also deduced in a recent study on recombination dynamics in powdered tellurium [44]. Moreover, the authors found that radiative recombination is dominant with 98% radiative yield at room temperature. Hence, we modeled the dynamics with radiative recombination (which accounts for the fluence dependence) and surface recombination (which accounts for the thickness dependence), and the diffusion process. By fitting the radiative recombination coefficient and surface recombination term, we obtained good agreements with experiments as seen in Fig. 2a and 2b for both thickness dependent and fluence dependent data. The radiative recombination coefficient was obtained as $1.9 \mp 0.1 \times 10^{-9}$ cm^3/s. Our value is lower than the 1.1×10^{-8} cm^3/s obtained by Bhaskar et al [44] but higher than other traditional direct bandgap semiconductors such as GaAs which has a value of ~7×10^{-10} cm^3/s at room temperature. The surface recombination velocity is found as $V_s = \frac{2 \times 10^6}{t}$ cm/s, where t is the thickness in nm. Typically, the Fuchs-Sondheimer theory was used to account for the thickness dependent electrical resistivity, which has a ~1/t dependence for t>>λ, where λ

is the mean free path [47,48]. The 1/t trend obtained from our modeling is likely a lumped effect from a number of phenomena such as scattering and possible thickness dependent surface defects.

Flakes with smaller thicknesses show different dynamics, and a transition occurs around 40 nm thickness as shown in Fig. 3a. The sign of the transmission signal starts flipping from positive to negative accompanied by a shorter time constant of decay. Comparing the 3500 nm probe and 5800 nm probe for the 40 nm flake, we see that after the change in sign from negative to positive for 5800 nm probe, the curves merge at about 50 ps. This shows that there are two distinct relaxation processes. As the thickness is reduced further, the signs for both probe wavelengths become negative and the lifetime is sub 20 ps, as seen in Fig. 3b for a 12 nm flake with 3500 nm probe (A 5800 nm probe, shown in Supplementary note 4, Fig. S2 [34], produces a very similar result). The simulation reproduces the fast relaxation well, as shown by the blue solid line in Fig. 3b. Two more flakes with thickness 13 and 17 nm produced similar results.

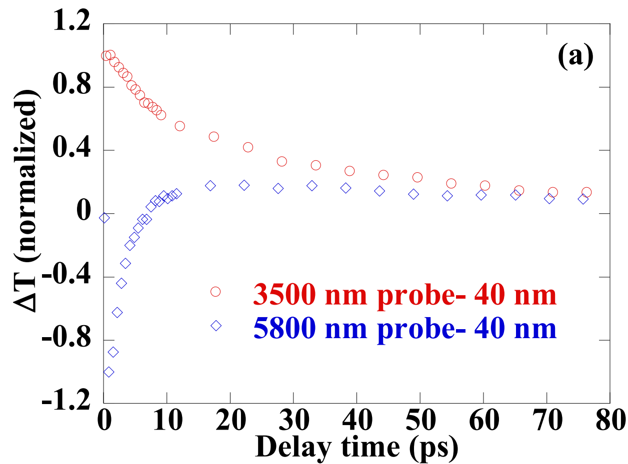

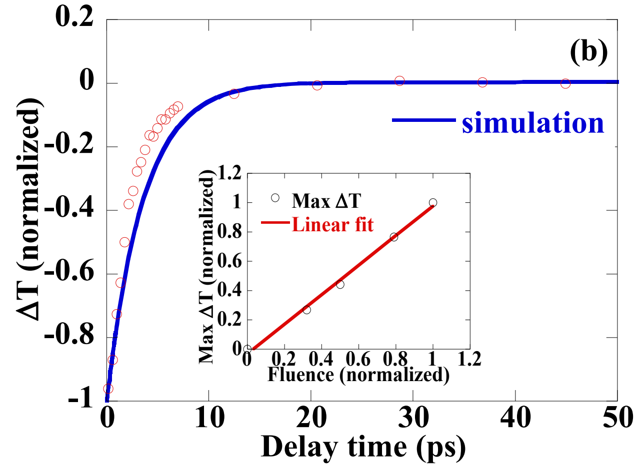

Fig. 3: (a) Relaxation dynamics in a 40 nm thick flake, showing positive sign (3500nm probe) and sign flipping (5800 nm probe). At delays greater than 50 ps, the curves merge together. (b) Relaxation dynamics in 12 nm flake following excitation by 800 nm pump and probing with 3500 nm. Inset shows pump fluence dependence along with linear fit, confirming absence of any non-linear effects. The blue solid line is from the diffusion-recombination simulation.

In thinner flakes, the observed relaxation is entirely due to carrier capture by surface trap states. The mobility of transistors made from solution grown tellurium was seen to sharply decrease below 20 nm thickness [20] and was ascribed to surface scattering and interface defects.. Such timescales have been previously related to fast capture of carriers by mid gap defect states in MoS_2 [49]. To ensure that the drastic change in the signal is not due to non-linear effects such as Auger recombination, we show the maximum change in transmission as a function of fluence and observe a linear trend as shown in the inset of Fig. 3b, which rules out such possibilities. A fluence test on relaxation time (Supplementary note 6, Fig. S4 [34]) revealed fluence independent relaxation which further suggests surface recombination as the dominant mechanism in thin flakes.

We also address the thickness dependence of the bandgap, as it is known to increase from bulk to monolayer [20]. The 12 nm flake for example is expected to show an increase of ~50 meV and have a

bandgap of ~0.4 eV. We measured the dynamics with a 2800 nm (0.44 eV), but did not observe any difference compared to the 3500 nm (0.35 eV) probe (Supplementary note 7, Fig. S5. [34]) We also performed a probe wavelength sweep near time delay of 0 ps (Supplementary note 7, Fig. S6. [34]) and found only weak features similar to the FTIR spectrum shown in Fig 1c, 14 nm flake. Hence we conclude that either the bandgap did not change as predicted or that the 3500 nm probe monitors the free carriers and hence does not show any difference compared to the near bandgap probe of 2800 nm, similar to probing with 5800 nm probe. Excitonic effects could play a role in the thin films as discussed earlier, however the exciton lifetimes are generally in the 100s of ps to ns range [50–52], unlike the short timescales in our measurements. Some studies found the lifetime to be in <10 ps at very low temperature of 4 K, but 100s of ps at room temperature [53,54]. Furthermore, timescales of <5 ps at room temperature was attributed to trapping of excitons by surface defects in MoS_2 [55]. Therefore, we conclude that even with possible exciton activity for the thin flakes, the surface defect assisted relaxation is the dominant process at room temperature.

The excitation and recombination processes can be summarized in Fig. 4. Fig. 4a describes thick flakes and Fig. 4b describes thin flakes. Before the arrival of the pump pulse (t < 0, left column), the material is at its ground state (p-type [20]). At the time of excitation, (t = 0, center column), the pump pulse completes populating the higher energy states, i.e. conduction band in the thick flakes and both conduction band and mid-gap trap states in the thin flakes. Intraband thermalization process (on the order of 100 fs in common 2D materials [56,57]) occurs within the time resolution of our experiment (500 fs). After rapid carrier-phonon scattering, carrier recombination occurs. In case of thin flakes, since the recombination proceeds through the many mid-gap trap states, it must necessarily be phonon assisted as shown, which explains why the recombination time is on the order the electron-phonon interaction times.

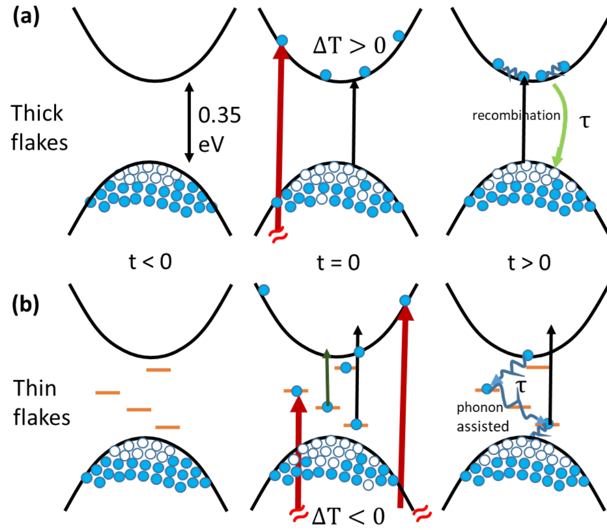

Fig. 4: Excitation and relaxation mechanism in thick flakes (upper 3 panels), where direct recombination plays a dominant role, and in thin flakes (10-20 nm, lower 3 panels), where the excited carriers recombine predominantly through several mid-gap surface trap states. The red arrow denotes the pump beam (800 nm), the black and dark green arrows represent the 3500 nm and 5800 nm probe respectively. The white circles are the holes and blue circles are the electrons. The orange bars are trap states.

The proposed ultrafast transmission mechanisms in Fig. 4 also explains the increase or decrease transmission in thick and thin flakes. The positive sign of the transmission signal (induced transmission) in thick flakes indicates Pauli blocking between initial and final states, thus indicating interband probing as shown in Fig. 4a. The 3500 nm probe monitors the valence band to conduction band transition, whereas the 5800 nm probe monitors inter-valence band transitions, several of which, in the mid-infrared region, have been found in literature [20,58–61]. On the other hand, thin flakes show a negative transmission signal (induced absorption), thereby indicating transitions from mid-gap trap states to the conduction band as shown in Fig. 4b. For the transition flake (40 nm flake, Fig 3a), the negative signal from the mid-gap trap states and the positive signal from the Pauli-blocking start to compete. The 3500 nm probe response is

dominated by interband transition, due to it being the primary strong transition, whereas the 5800 nm probe starts to encounter a superposition of responses from inter-valence band states and mid-gap trap states, producing a sign change.

Lastly we looked at the transient dynamics with pump and probe polarizations in the direction parallel to the c-axis. The absorption coefficient of the pump laser is different along the c-axis and perpendicular to it by a factor of 1.8 for 130 nm flake (see Supplementary note 3 [34]), and hence pumping and probing along the c-axis should produce a change in the slope of the relaxation due to different initial exited carrier concentration. We observe such a dependence as shown in Supplementary note 8, Fig S7 [34]. The thinner flakes did not show any directional dependence and reinforce the fluence independent surface recombination mechanism as shown in Supplementary note 8, Fig S8 [34].

In summary, we have performed ultrafast infrared transmission spectroscopy on tellurium flakes with thicknesses ranging from 12 nm to 160 nm and found a strong dependence of the recombination times on thickness. Thin flakes show a fast decay on the order of 20 ps, whereas thicker flakes have a decay in the 100s of ps range. The recombination mechanism in thin flakes was attributed to fast carrier capture by mid-gap defect states arising from surface defects and that in the thick flakes to radiative recombination. Recombination coefficients were extracted using a diffusion-recombination model. The fundamental carrier dynamics for tellurium thin films at room temperature aids in the understanding and better design of electronic and opto-electronic devices.

We acknowledge financial support from AFOSR/NSF under the EFRI2- DARE Grant EFMA-1433459 and NSF under the grant CMMI-1762698. We also thank Shouyuan Huang for preparing CaF_2 substrates.

References:

[1] G. Fiori, F. Bonaccorso, G. Iannaccone, T. Palacios, D. Neumaier, A. Seabaugh, S. K. Banerjee, and L. Colombo, Nat. Nanotechnol. **9**, 768 (2014).

[2] N. Briggs, S. Subramanian, Z. Lin, X. Li, X. Zhang, K. Zhang, K. Xiao, D. Geohegan, R. Wallace, L.-Q. Chen, M. Terrones, A. Ebrahimi, S. Das, J. Redwing, C. Hinkle, K. Momeni, A. van Duin, V. Crespi, S. Kar, and J. A. Robinson, 2D Mater. **6**, 022001 (2019).

[3] P. K. Venuthurumilli, P. D. Ye, and X. Xu, ACS Nano **12**, 4861 (2018).

[4] Q. Bao and K. P. Loh, ACS Nano **6**, 3677 (2012).

[5] P. Avouris, Nano Lett. **10**, 4285 (2010).

[6] F. Schwierz, Nat. Nanotechnol. **5**, 487 (2010).

[7] Q. H. Wang, K. Kalantar-Zadeh, A. Kis, J. N. Coleman, and M. S. Strano, Nat. Nanotechnol. **7**, 699 (2012).

[8] H. Liu, A. T. Neal, Z. Zhu, Z. Luo, X. Xu, D. Tománek, and P. D. Ye, ACS Nano **8**, 4033 (2014).

[9] F. Xia, H. Wang, and Y. Jia, Nat. Commun. **5**, 4458 (2014).

[10] Y. L. Chen, J. G. Analytis, J.-H. Chu, Z. K. Liu, S.-K. Mo, X. L. Qi, H. J. Zhang, D. H. Lu, X. Dai, Z. Fang, S. C. Zhang, I. R. Fisher, Z. Hussain, and Z.-X. Shen, Science **325**, 178 (2009).

[11] L. Cheng and Y. Liu, J. Am. Chem. Soc. **140**, 17895 (2018).

[12] Z. Yu, Z.-Y. Ong, S. Li, J.-B. Xu, G. Zhang, Y.-W. Zhang, Y. Shi, and X. Wang, Adv. Funct. Mater. **27**, 1604093 (2017).

[13] J. O. Island, G. A. Steele, H. S. J. van der Zant, and A. Castellanos-Gomez, 2D Mater. **2**, 011002 (2015).

[14] C. Durand, X.-G. Zhang, S. M. Hus, C. Ma, M. A. McGuire, Y. Xu, H. Cao, I. Miotkowski, Y. P. Chen, and A.-P. Li, Nano Lett. **16**, 2213 (2016).

[15] A. Reina, X. Jia, J. Ho, D. Nezich, H. Son, V. Bulovic, M. S. Dresselhaus, and J. Kong, Nano Lett.

9, 30 (2009).

[16] A. Roy, H. C. P. Movva, B. Satpati, K. Kim, R. Dey, A. Rai, T. Pramanik, S. Guchhait, E. Tutuc, and S. K. Banerjee, ACS Appl. Mater. Interfaces **8**, 7396 (2016).

[17] J. Kang, J. D. Wood, S. A. Wells, J.-H. Lee, X. Liu, K.-S. Chen, and M. C. Hersam, ACS Nano **9**, 3596 (2015).

[18] Y.-C. Lin, W. Zhang, J.-K. Huang, K.-K. Liu, Y.-H. Lee, C.-T. Liang, C.-W. Chu, and L.-J. Li, Nanoscale **4**, 6637 (2012).

[19] Y. Lee, S. Bae, H. Jang, S. Jang, S.-E. Zhu, S. H. Sim, Y. Il Song, B. H. Hong, and J.-H. Ahn, Nano Lett. **10**, 490 (2010).

[20] Y. Wang, G. Qiu, R. Wang, S. Huang, Q. Wang, Y. Liu, Y. Du, W. A. Goddard, M. J. Kim, X. Xu, P. D. Ye, and W. Wu, Nat. Electron. **1**, 228 (2018).

[21] Y. Wang, R. de Souza Borges Ferreira, R. Wang, G. Qiu, G. Li, Y. Qin, P. D. Ye, A. Sabbaghi, and W. Wu, Nano Energy **57**, 480 (2019).

[22] M. Amani, C. Tan, G. Zhang, C. Zhao, J. Bullock, X. Song, H. Kim, V. R. Shrestha, Y. Gao, K. B. Crozier, M. Scott, and A. Javey, ACS Nano **12**, 7253 (2018).

[23] S. Berweger, G. Qiu, Y. Wang, B. Pollard, K. L. Genter, R. Tyrrell-Ead, T. M. Wallis, W. Wu, P. D. Ye, and P. Kabos, Nano Lett. **19**, 1289 (2019).

[24] G. Qiu, Y. Wang, Y. Nie, Y. Zheng, K. Cho, W. Wu, and P. D. Ye, Nano Lett. **18**, 5760 (2018).

[25] W. Wu, G. Qiu, Y. Wang, R. Wang, and P. Ye, Chem. Soc. Rev. **47**, 7203 (2018).

[26] C. Chen, I. Vasudevan, Z. Du, X. Xu, and L. Pan, Appl. Phys. Lett. **112**, 253105 (2018).

[27] B. T. Spann and X. Xu, Appl. Phys. Lett. **105**, 083111 (2014).

[28] L. Guo and X. Xu, J. Heat Transfer **136**, 122401 (2014).

[29] F. Ceballos and H. Zhao, Adv. Funct. Mater. **27**, 1604509 (2017).

[30] V. Iyer, Y. P. Chen, and X. Xu, Phys. Rev. Lett. **121**, 026807 (2018).

[31] S. Hunsche, K. Wienecke, T. Dekorsy, and H. Kurz, Phys. Rev. Lett. **75**, 1815 (1995).

[32] N. Kamaraju, S. Kumar, M. Anija, and A. K. Sood, Phys. Rev. B **82**, 195202 (2010).

[33] S. Tutihasi, G. G. Roberts, R. C. Keezer, and R. E. Drews, Phys. Rev. **177**, 1143 (1969).

[34] See Supplementary Material at [URL] for details of the material synthesis, Raman characterization, experimental setup, simulation and additional experiments.

[35] A. S. Pine and G. Dresselhaus, Phys. Rev. B **4**, 356 (1971).

[36] R. M. Martin, G. Lucovsky, and K. Helliwell, Phys. Rev. B **13**, 1383 (1976).

[37] Y. Pan, S. Gao, L. Yang, and J. Lu, Phys. Rev. B **98**, 085135 (2018).

[38] H. M. Hill, A. F. Rigosi, C. Roquelet, A. Chernikov, T. C. Berkelbach, D. R. Reichman, M. S. Hybertsen, L. E. Brus, and T. F. Heinz, Nano Lett. **15**, 2992 (2015).

[39] K. Yao, A. Yan, S. Kahn, A. Suslu, Y. Liang, E. S. Barnard, S. Tongay, A. Zettl, N. J. Borys, and P. J. Schuck, Phys. Rev. Lett. **119**, 087401 (2017).

[40] A. Ferreira da Silva, N. Veissid, C. Y. An, I. Pepe, N. Barros de Oliveira, and A. V. Batista da Silva, Appl. Phys. Lett. **69**, 1930 (1996).

[41] D. Redfield, Phys. Rev. **100**, 1094 (1955).

[42] V. A. Vis, J. Appl. Phys. **35**, 360 (1964).

[43] A. Bringer and G. Nimtz, Phys. Status Solidi **46**, 235 (1971).

[44] P. Bhaskar, A. W. Achtstein, M. J. W. Vermeulen, and L. D. A. Siebbeles, J. Phys. Chem. C **123**, 841 (2019).

[45] S. M. Sze and K. K. Ng, *Physics of Semiconductor Devices* (John Wiley & Sons, New Jersey, 2006).

[46] J. S. Blakemore, J. W. Schultz, and K. C. Nomura, J. Appl. Phys. **31**, 2226 (1960).

[47] E. H. Sondheimer, Adv. Phys. **1**, 1 (1952).

[48] F. Lacy, Nanoscale Res. Lett. **6**, 636 (2011).

[49] H. Wang, C. Zhang, and F. Rana, Nano Lett. **15**, 339 (2015).

[50] L. Yuan and L. Huang, Nanoscale **7**, 7402 (2015).

[51] T. Wang, Y. Zhang, Y. Liu, J. Li, D. Liu, J. Luo, and K. Ge, J. Phys. Chem. C **122**, 18651 (2018).

[52] N. Kumar, Q. Cui, F. Ceballos, D. He, Y. Wang, and H. Zhao, Nanoscale **6**, 4915 (2014).

[53] T. Korn, S. Heydrich, M. Hirmer, J. Schmutzler, and C. Schüller, Appl. Phys. Lett. **99**, 102109 (2011).

[54] C. Robert, D. Lagarde, F. Cadiz, G. Wang, B. Lassagne, T. Amand, A. Balocchi, P. Renucci, S. Tongay, B. Urbaszek, and X. Marie, Phys. Rev. B **93**, 205423 (2016).

[55] H. Shi, R. Yan, S. Bertolazzi, J. Brivio, B. Gao, A. Kis, D. Jena, H. G. Xing, and L. Huang, ACS Nano **7**, 1072 (2013).

[56] J. M. Dawlaty, S. Shivaraman, M. Chandrashekhar, F. Rana, and M. G. Spencer, Appl. Phys. Lett. **92**, 042116 (2008).

[57] Z. Nie, R. Long, L. Sun, C. C. Huang, J. Zhang, Q. Xiong, D. W. Hewak, Z. Shen, O. V. Prezhdo, and Z. H. Loh, ACS Nano **8**, 10931 (2014).

[58] E. Bangert, D. Fischer, and P. Grosse, Phys. Status Solidi **59**, 419 (1973).

[59] D. Fischer, E. Bangert, and P. Grosse, Phys. Status Solidi **55**, 527 (1973).

[60] R. Enderlein and A. Hache, Phys. Status Solidi **60**, 739 (1973).

[61] J. Qiao, Y. Pan, F. Yang, C. Wang, Y. Chai, and W. Ji, Sci. Bull. **63**, 159 (2018).